Section 4

Field measurements

Limnol. Oceanogr., 34(8), 1989, 1614–1622

Use of the radiance distribution to measure the optical absorption coefficient in the ocean

K. J. Voss
Department of Physics, University of Miami, Coral Gables, Florida 33124

Abstract

Recent advances in instrumentation have enabled the accurate measurement of radiance distribution profiles. These measurements with the electro-optic radiance distribution camera system (RADS) can be used to explore theoretical treatments relating the radiance distribution to inherent properties such as absorption. I use a radiance distribution cast to obtain a profile of the optical absorption coefficient. Because this measurement of absorption is not direct, but rather is derived from the radiance distribution data, analysis of the possible sources of error is detailed, along with the advantages and disadvantages of the method.

Measurement of the spectral optical absorption coefficient is of fundamental importance in ocean optics. As an inherent optical property (one that does not depend on the illumination characteristics of the ambient light field, Preisendorfer 1976), along with the scattering function and beam attenuation coefficient, it describes the fundamental interaction of light with seawater. Although an important optical property, it has not lent itself to easy and routine field measurement. There are several techniques that hold promise for measuring small volumes of seawater, including photoacoustics (Voss and Trees 1987), the "shiny tube transmissometer" (Zaneveld et al. 1988), and integrating sphere (Fry and Kattawar 1988). Few methods lend themselves to measurement of the average spectral optical absorption coefficient for large (m^3) sample volumes.

Use of Gershun's law (Gershun 1939) to measure absorption in seawater allows measurement of the average spectral optical absorption coefficient (a) for large sample volumes; however, its use requires care and can be subject to several artifacts, both instrumental and environmental. Gershun's law uses conservation of energy in the ambient light field to derive a. I will discuss this in greater detail later, but for now it suffices to mention that the downwelling and upwelling scalar irradiance coefficients, E_{0d} and E_{0u}, must be measured along with the downwelling and upwelling vector irradiance coefficients, E_d and E_u, as functions of depth. In most instruments these measurements are performed by separate sensors that must maintain their intercalibration (Højerslev 1973). Recent advances in measuring the radiance distribution (Voss 1989) allow its measurement to occur with sufficient resolution and accuracy to permit calculation of E_{0d}, E_{0u}, E_d, and E_u (*see list of symbols*). The primary advantage of measuring these quantities with the radiance distribution is reduction of the number of

Acknowledgments

This work was supported by Office of Naval Research contract N00014-85-K-005. I also acknowledge the help of Albert Chapin in collecting the data and Bess Ward in allowing me to participate in her cruise on the RV *R.G. Sproul* (sponsored by NSF OCE86-14470), on which these data were obtained. I also thank Roswell Austin for his guidance and many fruitful conversations.

sensors required and elimination of possible drifts in absolute intercalibrations between sensors. It also allows quantification of possible sources of error in this measurement, while allowing a general analysis of the effects of errors in measurement of these quantities (E_d, E_u, E_{0u}, and E_{0d}) on the calculation of a.

Here I review the theoretical basis for measuring a with Gershun's law, show the results of a sample water profile measured with this method and radiance distribution data, and then analyze sources of error in this measurement.

Theory of Gershun's law

Gershun's law uses conservation of energy to show

$$aE_0 = -\text{div } E \tag{1}$$

where E_0 is the total scalar irradiance,

$$E_0 = E_{0d} + E_{0u},$$

div the divergence operator,

$$\text{div} = \frac{\partial}{\partial x} + \frac{\partial}{\partial y} + \frac{\partial}{\partial z},$$

and E the net or vector irradiance,

$$E = E_d - E_u.$$

The first approximation to be applied to enable use of this equation in the ocean to measure a is to assume that lensing and shadowing effects are absent; in other words, the irradiances are functions of depth only. This allows the divergence to be simplified by making the derivatives with y and x equal to zero. Gershun's law then simplifies to (Preisendorfer 1976)

$$aE_0 = -\frac{dE}{dz} \text{ or } a = -\frac{1}{E_0}\frac{dE}{dz}. \tag{2}$$

The average cosine, μ, relates E and E_0 for a given radiance distribution. It is defined by

$$\mu(z) = \frac{E(z)}{E_0(z)}.$$

With this relationship, Eq. 2 can be expanded to

$$a = -\frac{1}{E_0(z)}\frac{d}{d(z)}[\mu(z)E_0(z)] \tag{3}$$

Significant symbols

a	Absorption coefficient, m^{-1}
c	Beam attenuation coefficient, m^{-1}
E_{0d}, E_{0u}	Downwelling and upwelling scalar irradiance, $\mu W\ cm^{-2}\ nm^{-1}$
E_d, E_u	Downwelling and upwelling vector irradiance, $\mu W\ cm^{-2}\ nm^{-1}$
E	Net, or vector, irradiance, $\mu W\ cm^{-2}\ nm^{-1}$
E_0	Total scalar irradiance, $\mu W\ cm^{-2}\ nm^{-1}$
K_{Ed}, K_{E0}	Downwelling and scalar diffuse attenuation coefficients
μ	Average cosine
μ_d, μ_u	Downwelling and upwelling average cosine
z	Depth, m
$L(\theta, \psi, z)$	Radiance, $\mu W\ cm^{-2}\ nm^{-1}\ sr^{-1}$
Δ(quantity)	Error in quantity

$$a = -\frac{\mu(z)}{E_0(z)}\frac{dE_0(z)}{d(z)} - \frac{d\mu(z)}{d(z)}. \tag{4}$$

The asymptotic region is defined as that region where the shape of the radiance distribution does not change, $\mu(z) = \mu$, and therefore $d\mu(z)/dz$ is zero (Preisendorfer 1959). Also in the asymptotic region the diffuse attenuation coefficients for vector and scalar irradiance are equal (Preisendorfer 1959). In this region

$$\frac{dE(z)}{d(z)} = \mu\frac{dE_0}{d(z)},$$

and Eq. 4 and 2 are equivalent.

These equations, specifically Eq. 2 and 4, lead to the measurement techniques by which Gershun's law can be used to measure the spectral absorption coefficient. The first requirement is measurement of E_0 and E at various depths. Two methods may be involved; the first is through use of Eq. 2 and requires closely spaced measurements of E. Depths must be closely spaced since dE/dz must be determined for depth intervals for which the shape of the radiance distribution does not change significantly; μ (and therefore E_0) need only be measured at depths for which the absorption coefficient is required. In the second method, Eq. 4 is used and closely spaced measurements of E_0 and E must be obtained since both the change in E_0 and the change of μ with depth are required.

The above equations can also be used to determine $E_0(z)$. Equation 4 can be integrated to obtain (Stavn 1987):

$$E_0(z) = E_0(0)\frac{\mu(z)}{\mu(0)}\exp\left[-\int_0^z \frac{a(z')}{\mu(z')}\,dz'\right]. \quad (5)$$

Equation 5 is of limited use, since to obtain $E_0(z)$ at any depth requires knowledge of $E_0(z')$ and $E(z')$ at all depths, z', less than z in order to determine $\mu(z')$.

Measurement with radiance distribution

Recent developments in measuring the spectral radiance distribution (Voss 1988) through use of the electro-optic radiance distribution camera system (RADS) have led to its feasibility in measuring the absorption coefficient. RADS uses two electro-optic cameras with fisheye lenses to measure the complete radiance distribution at a given depth and a given wavelength and another camera system to measure the downwelling sky radiance distribution at the surface for that wavelength. The upwelling or downwelling spectral radiance distribution at each depth is measured quickly (<1 s); however, at present, transmitting the image to the surface requires 2 min per image. Thus, a cast with six depths sampled requires 0.5 h. The validity of assuming a constant light source for the cast is determined by using the surface radiance camera to investigate changes in the sky or solar radiance during the data cast. Although the limited sampling rate reduces the effectiveness of the use of RADS in routine measurement of the absorption coefficient in the ocean, the angular resolution of the data obtained allows investigation into possible consequences of instrumental errors and environmental conditions on the absorption measurement. RADS is therefore most useful as a tool to investigate various aspects of radiative transfer, such as the use of apparent optical properties to obtain inherent optical properties and to investigate radiative transfer models with the high angular resolution of RADS.

During a cruise off San Diego, RADS was used to collect radiance distribution data during a hydrocast. The data presented here are the results of this cast and a cast with the Vislab spectral transmissometer (VLST, Petzold and Austin 1968). The VLST is a beam transmissometer which allows the beam attenuation coefficient, c, at five different visible wavelengths to be measured. This transmissometer is a cylindrically limited design, with a forward angle acceptance of <1.5°. All beam transmissometer data presented are at 490 nm, obtained with a 10-nm bandwidth. For the RADS data presented, the downwelling radiance data were taken at 502.6 nm with a 25.5-nm bandwidth, and the upwelling radiance data were taken at 504.8 nm with a 26.0-nm bandwidth. No effort was made to correct for this slight wavelength mismatch in the data analysis.

A single cast was chosen, for which measurements of the radiance distribution at depths of 20.0, 24.8, 29.9, 44.8, 49.6, and 54.7 m were available. These measurements were obtained between 1248 PST (for the start of the 54.7-m sample) and 1328 PST (for the end of the 20-m sample). Measurements were also obtained at 35 and 40 m but were discarded because of pixel saturation in the images.

Figure 1 shows the reduced radiance distribution for these casts. In the panels of this figure the image on the left is the downwelling radiance distribution; the image on the right is the upwelling radiance distribution. These images are best thought of as radiance distribution maps. The projection of these maps is as follows: the zenith angles for the images are directly proportional to the radial distance from the center of the image. The relative azimuthal directions are obtained directly by the azimuthal position in the image. The relative phase of the azimuthal direction for the downwelling and upwelling images is as follows: if one sets the azimuthal angle (ψ) in the downwelling radiance distribution image equal to zero for the top of the image, ψ increases in a clockwise direction. For the upwelling radiance distribution image ψ increases in a counterclockwise direction. For example, the top of the images correspond to the same ψ direction in both the upwelling and downwelling images (0°). The left-hand side of the downwelling image corresponds to the right-hand side of the upwelling image and vice versa. The bottoms of both images cor-

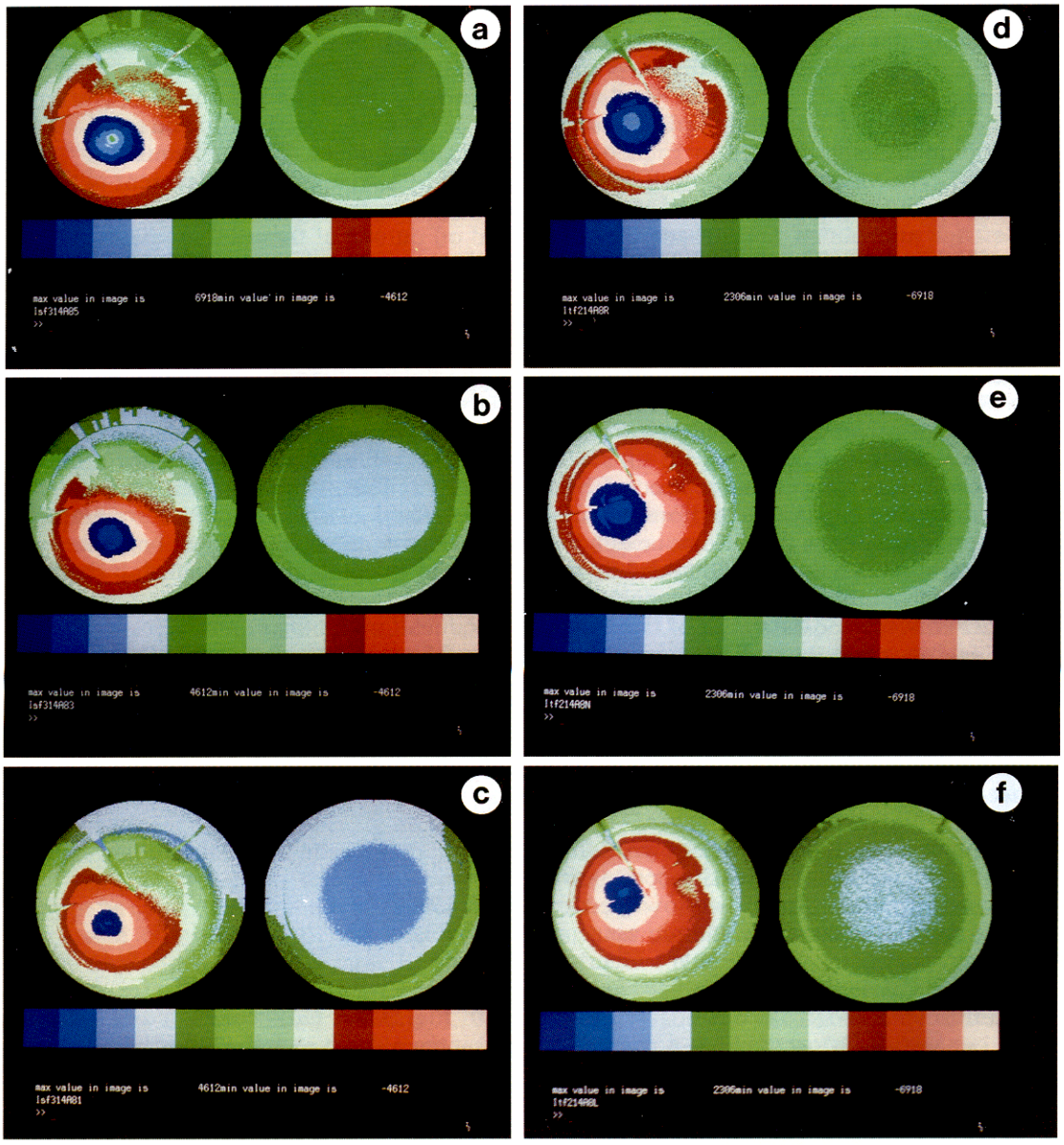

Fig. 1. Radiance distribution profile, obtained on 14 October 1988 at 33°43.9′N, 118°47.5′W from the RV *R. G. Sproul.* Left image is the downwelling radiance distribution; right image is the upwelling radiance distribution: a—20 m; b—24.8 m—29.9 m; d—44.8 m; e—49.6 m; f—54.7 m.

respond to the same ψ direction (180°). As a final description, if one were to take each figure and fold it over along the centerline between the images, the edge of the images would be joined correctly.

The images are displayed in false color, with each color representing a $10^{0.25}$ step (2.5 dB) in radiance (in units of μW cm^{-2} sr^{-1} nm^{-1}). The color bars correspond to the color mapping, with the lowest radiance at the left and the higher values at the right. Because only 16 colors were available, the scales overlap in regions of high radiance. In Fig. 1a–c, the minimum color scale is at 10^{-2} μW cm^{-2} sr^{-1} nm^{-1}; for Fig. 1d–f, the minimum color scale is at 10^{-3} μW cm^{-2}

sr^{-1} nm^{-1}. If Fig. 1a is used as an illustration, the center of the image of the upwelling radiance distribution has radiance values between 10^{-1} and $10^{-1.25}$ $\mu W\ cm^{-2}\ sr^{-1}\ nm^{-1}$ (the center of the upwelling image has the minimum radiance values in each of the images). The values in the upwelling radiance distribution increase toward their outside edge and match the 90° zenith angle values in the downwelling radiance distribution. The bright portion of the downwelling image is the direct solar component, and the radiance values here reach the range of 10^3–$10^{3.25}$ $\mu W\ cm^{-2}\ sr^{-1}\ nm^{-1}$ (the very small green spot in the center of the solar component); the other images follow similarly.

These images were also processed with an additional step beyond the radiometric calibration. Because the data did not extend to 90° zenith in both the upwelling and downwelling images, a routine to interpolate the images between the data edge of the downwelling image and the upwelling image was devised. A logarithmic least-squares fit was performed on 5° sections of ψ and this line used to fill in data along the edges, which then satisfied the condition that the radiance distribution be continuous between the upwelling and downwelling images. An edge effect appears in the raw data downwelling image due to a neutral density coating installed on the instrument window (needed to reduce the intrascene dynamic range of the camera system, Voss 1989). A logarithmic least-squares fit was also used in this region to smooth across this edge effect in the image (which occurs at ~45° zenith). These two steps are necessary to allow accurate calculation of E_d, E_u, E_{0d}, and E_{0u} from these images.

Several qualitative features are evident in these images. As the depth increases, the portion of the downwelling image relating to the solar component decreases in value and becomes less peaked (fewer contours per angular region). Another feature of the downwelling images is that they get much more symmetric and have much less variation in radiance values with depth [in the image at 20.0 m (Fig. 1a) the radiance values range over 32.5 dB, while in the image at 54.7 m (Fig. 1f) the values range over 22.5 dB]. The upwelling images show no large-scale change, but tend to decrease evenly overall.

Another qualitative feature of these images is the evidence of a ship and cable shadow in the images. The instrument is supported by a triangular arrangement of three cables, with the instrument electrical cable tied off on one of these cables. These show in the images as three radial stripes [e.g. in the image at 54.7 m (Fig. 1f) these stripes occur at ψ of ~35°, 260°, and 330°]. The ship shadow also causes an obvious effect in the downwelling image [most clearly evident in the images at 49.6 m (Fig. 1e) and 54.7 m (Fig. 1f) as the intrusions of low radiance values into high radiance areas at ψ of 45°]. This instrument shows the first-order effects of ship shadow quite plainly, and some of these images will be used elsewhere to calculate the effect of ship shadow on the irradiance and radiances measured.

Values for the $E_0(z)$ and $E(z)$ were obtained from these images through use of the equations

$$E_{0d}(z) = \int_0^{2\pi} d\psi \int_0^{90} \sin(\theta)\, d\theta\, L(\theta, \psi, z)$$

and

$$E_d(z) = \int_0^{2\pi} d\psi \cdot \int_0^{90} \sin(\theta)\, d\theta\, L(\theta, \psi, z) \cos(\theta)$$

with $E_{0u}(z)$ and $E_u(z)$ calculated from similar integrals, but over the lower hemisphere ($90 \le \theta \le 180$). Because the data existed as discrete values, these integrals were performed as numerical sums, with each pixel weighted by the solid angle it represented. Table 1 compiles these data, along with the upwelling and downwelling average cosines (calculated using $\mu_d = E_d/E_{0d}$ and $\mu_u = E_u/E_{0u}$). From these values, the absorption can be calculated with two methods outlined previously. The first (using Eq. 2) is shown in Table 2 as $a(1)$ and the second (using Eq. 4) as $a(2)$. The differentials in the equations were obtained by fitting the linear variation of the natural logarithm of the values concerned (E_0, E_d, and μ for the depth above,

Table 1. Downwelling and upwelling irradiance, downwelling and upwelling scalar irradiance, and downwelling and upwelling average cosines for depths sampled.

Depth (m)	$E_d(z)$	$E_{0d}(z)$	$E_u(z)$	$E_{0u}(z)$	$\mu_d(z)$	$\mu_u(z)$
	(μW cm^{-2} nm^{-1})					
20.0	16.75	23.11	0.4884	1.292	0.725	0.378
24.8	9.338	13.04	0.3300	0.8517	0.716	0.387
29.9	6.295	8.775	0.2118	0.5497	0.717	0.385
44.8	1.733	2.307	0.06583	0.1597	0.751	0.412
49.6	1.557	2.071	0.05176	0.1295	0.752	0.400
54.7	1.059	1.401	0.03891	0.09596	0.756	0.405

depth below, and central depth) with depth. The functional form was assumed to be logarithmic due to the exponential relationship of $\mu(z)$ and $E_0(z)$ with z detailed in Eq. 5. The absorptions obtained with these two methods are close to equal (the maximum difference is 2.3%). Also shown in this table are both $\mu(z)$ and $d\mu(z)/dz$. The magnitude of $d\mu(z)/dz$ was quite small at all of these depths, reaching a maximum of 2.6% of the absorption at 29.9 m. One would expect that $d\mu(z)/dz$ would be larger at depths <10 m, where the radiance distribution is changing rapidly; however, due to the large dynamic range in the radiance distribution at these depths, this cannot be measured with RADS at this time.

During this cruise no alternate method of measuring the spectral absorption coefficient was available, so this measurement cannot be compared directly. However, one can use a combination of the absorption coefficient and the beam attenuation coefficient to interrelate to historical data. Table 3 illustrates the scattering coefficient, obtained through the closure relation, the single scattering albedo, and the scattering to absorption ratio. Kirk (1981) reported results of a Monte-Carlo study of the relationships between optical properties in water with varying inherent properties. These results are useful in that they provide a reference for the predicted average cosine and reflectance as a function of b/a. These results generally agree with my measurements (e.g. my measurement at 24.8 m indicated a b/a of 3.84). If one interpolates figure 2 of Kirk for this value of b/a, μ is between 0.70 and 0.63 (my value was 0.648) and reflectance is 0.03 (my value was 0.035).

Table 2. Total average cosine, change in average cosine, the absorption coefficient calculated with Eq. 2 [$a(1)$] and the absorption coefficient calculated with Eq. 4 [$a(2)$].

Depth (m)	$\mu(z)$	$d\mu(z)/dz$	$a(1)$	$a(2)$
			(m^{-1})	
20.0	0.666	—	—	—
24.8	0.648	−0.00139	0.0648	0.0643
29.9	0.652	0.00145	0.0553	0.0553
44.8	0.676	0.00162	0.0505	0.0504
49.6	0.684	0.00049	0.0341	0.0349
54.7	0.681	—	—	—

Error analysis

There are several possible sources for error in these or any measurement of the irradiance values which can affect the calculation of a.

The first source of error to be investigated is the effect of a limited dynamic range (~30 dB for the downwelling radiance distribution) on the calculation of the scalar and vector irradiance coefficients. The upwelling light field is characteristically flat, with much lower intrascene dynamic range; thus, it is much less likely to be affected by this problem. The downwelling radiance distribution has much more intrascene dynamic range and hence is the measurement for which great care must be taken. Although

Table 3. Scattering coefficient, calculated using the closure relation ($b = c - a$), single scattering albedo ($\omega = b/c$), and ratio of b/a.

Depth (m)	$b(z)$ (m^{-1})	ω	b/a
24.8	0.249	0.793	3.843
29.9	0.251	0.819	4.539
44.8	0.156	0.754	3.089
49.6	0.167	0.833	4.897

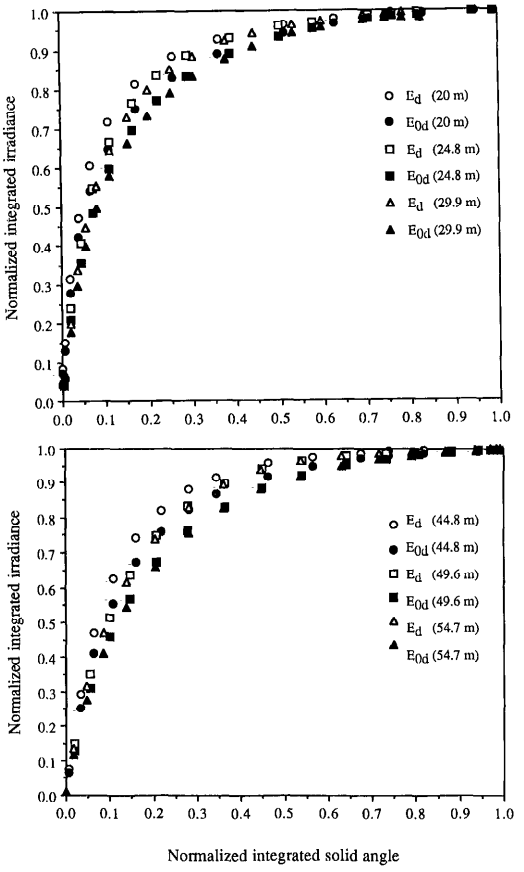

Fig. 2. Plot of the normalized integrated solid angle vs. integrated normalized downwelling irradiance, illustrating the concentration of irradiance near zenith.

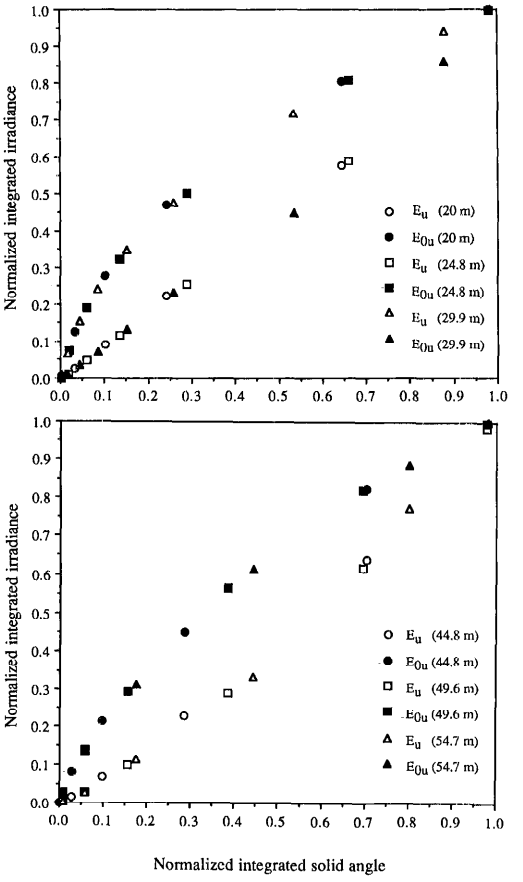

Fig. 3. Plot of the normalized integrated solid angle vs. integrated normalized upwelling irradiance.

steps can be taken to ensure that no pixels in the field are saturated, the great dynamic range means that some of the pixels will be in the dark noise of the imager. Figure 2 illustrates the relative importance of the levels of radiance in calculating the scalar and vector irradiance. In this figure, the irradiance is integrated, starting at the pixels with the highest values of radiance and progressing to the lowest. As can be seen, at worst (scalar irradiance at 54.7 m) 50% of the irradiance is calculated from the 12% of solid angle with the higher radiance values, while 90% of the irradiance is calculated from 47% of the solid angle. For this cast, on average, 50% of the irradiance is calculated from 8% of solid angle, and 90% of the irradiance is calculated from 37% of solid angle. Thus if 10–20% of the lowest solid angle in the image is neglected, the irradiance values will only be changed by a negligible amount.

The same cannot be said for the upwelling field, as shown in Fig. 3. Here the higher radiance regions of solid angle do not dominate the irradiances. Although the limited intrascene dynamic range of this field allows careful measurement of the whole area, all of the lower hemisphere must be measured if accurate values for scalar and vector irradiance are to be obtained.

The next source of possible error is in the determination of μ with limited field-of-view sensors. Figures 4 and 5 illustrate the downwelling and upwelling average cosine as a function of integration angle. In the case of the downwelling (upwelling) average cosine, the irradiances used to find μ are integrated from zenith (nadir) to the given angle. In

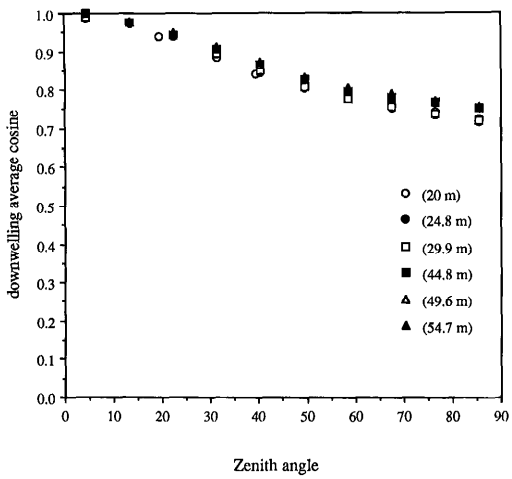

Fig. 4. Downwelling average cosine as a function of included solid angle.

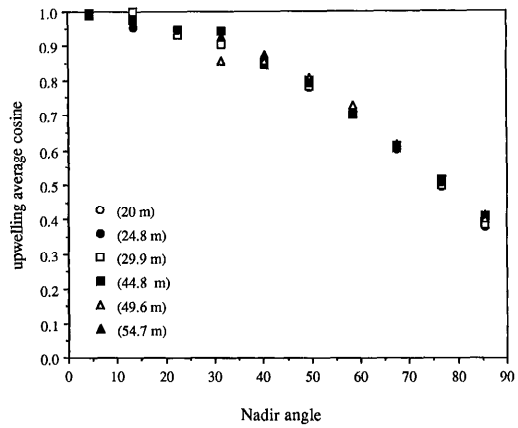

Fig. 5. Upwelling average cosine as a function of included solid angle.

the downwelling case, μ changes rapidly at the beginning but tends toward an asymptotic value at greater integration angles because the angles near 90° have radiance values low relative to the zenith, and thus affect E_0, E, and μ to a lesser degree. The curve shown in Fig. 4 has been fitted with a polynomial and the slope calculated. In this manner, the rate of change of μ at each angle can be determined. The rate of change in this case (at 80°) is 0.08% per degree. Thus, measurement of the irradiance values with collectors limited to an 85° field of view leads to a 0.4% error in μ.

In the case of the upwelling light field the effect is much stronger. As can be seen in Fig. 5, the calculated upwelling average cosine changes rapidly with angle because the large values of radiance in the upwelling distribution occur near 90°, where they affect E_0 strongly but do not add significantly to E due to the cosine weighting factor. If this equation is fitted with a polynomial and the rate of change determined, an error of 1.2% per degree (at 80°) is found. This leads to an error of 6% in μ for an 85° field of view. Thus, in the upwelling field more care must be taken to correctly measure the scalar and vector irradiance near 90° to avoid large errors in measurement that can propagate into the calculation of a.

To determine the total error in the measurement of a, I chose Eq. 2 with the assumption that μ was not changing rapidly. The equation describing the error is then

$$\Delta a = (\Delta\mu)\frac{\mathrm{d}\ln(E_0)}{\mathrm{d}(z)} + \mu\Delta\frac{\mathrm{d}\ln E_0}{\mathrm{d}(z)}.$$

Calculating the error in this case shows the relative error in the measurement of the radiance distribution, and thus μ is 6% (Voss and Zibordi 1989). The error in determining the slopes (three points used in the regression) can be determined by the standard error of the slope; the average was found to be 15% for the four points calculated, which implies a total error of 21% in the measurement of a.

These measurements can also be used to estimate the probable errors in other instrumental configurations and can be made most accurately by combining the radiance distribution data presented with the exact parameters of the specific instruments. Two examples are presented here. In the first example, an instrument is used that measures only the downwelling parameters (but does so perfectly); it is assumed that these will dominate the resulting μ, E, and E_0. In this case the a which one would calculate can be found simply from the tables of data presented. The differences between this case and the complete calculation range from 10 to 16%. This result shows the relative dominance of the downwelling component in the calculation of a with this method.

In the second case, an instrument is used that measures both upwelling and downwelling irradiance, but only to 85° zenith

angle in the downwelling case and 85° nadir angle in the upwelling case. In such an example, μ_d would be off by 0.4% and μ_u by 6%. It is difficult to estimate how dE_0/dz would be affected, but K_{Ed} and K_{E0} at 24.8 m are quite similar ($K_{Ed} = 0.0988$ m^{-1}, $K_{E0} = 0.0976$ m^{-1}, implying K will probably be affected to only a small degrec (2%). In this case the total error for the measured a would be ~4%, taking into account the domination of E_d and μ_d in E and μ. In both examples, the instruments were assumed to determine the measured parameters exactly; additional instrumental errors would be additive.

Another possible source of error which must be taken into account is that due to extra sources of radiance in the measured spectral band. Examples of possible sources are Raman scattering (Stavn 1988), fluorescence (Gordon 1979), etc. In the spectral region measured in this example (500 nm), Raman scattering is probably negligible; however, it would be an important factor at longer wavelengths and would probably limit this method's usefulness. Although the common phytoplankton fluorescence occurs at wavelengths around 685 nm and certain types of dinoflagellates can fluoresce in the green (Shapiro et al. 1989), the effect at this wavelength (500 nm) would probably be negligible. This green fluorescence could become important at wavelengths around 550 nm where the total irradiance of the ambient light is reduced due to increased attenuation; at wavelengths >600 nm other phytoplankton could contribute significantly to the background irradiance.

Conclusions

These measurements illustrate the use of the radiance distribution to measure the optical absorption coefficient profile. Instrumental error was analyzed and found to be ~21%. Although this is a good method of measuring the bulk absorption coefficient, measurement of absorption is not the major purpose of an instrument such as RADS. RADS, with its fine angular resolution, can be used to determine the experimental limitations of other instruments with known measurement characteristics. Data from RADS can also be used to provide experimental tests of radiative transfer models and verifications of these models and their corresponding assumptions.

References

FRY, E. S., AND G. W. KATTAWAR. 1988. Measurement of the absorption coefficient of ocean water using isotropic illumination, p. 142–148. *In* Ocean Optics 9, Proc. SPIE **925**.

GERSHUN, A. 1939. The light field. J. Math. Phys. **18**: 51–151.

GORDON, H. R. 1979. Diffuse reflectance of the ocean: The theory of its augmentation by chlorophyll *a* fluorescence at 685 nm. Appl. Opt. **18**: 1161–1166.

HØJERSLEV, N. K. 1973. Inherent and apparent optical properties of the western Mediterranean and the Hardangerfjord. Univ. Copenhagen Inst. Phys. Oceanogr. Rep. 21, p. 1–26.

KIRK, J. T. O. 1981. Monte Carlo study of the nature of the underwater light field in, and the relationships between optical properties of, turbid yellow waters. Aust. J. Mar. Freshwater Res. **32**: 517–532.

PETZOLD, T. J., AND R. W. AUSTIN. 1968. An underwater transmissometer for ocean survey work. Scripps Inst. Oceanogr. SIO Ref. 68-9.

PREISENDORFER, R. W. 1959. Theoretical proof of the existence of characteristic diffuse light in natural waters. J. Mar. Res. **18**: 1–9.

———. 1976. Hydrologic optics V. 1. NTIS PB-259793/8ST, Springfield, VA.

SHAPIRO, L. P., E. M. HAUGEN, AND E. J. CARPENTER. 1989. Occurrence and abundance of green-fluorescing dinoflagellates in surface waters of the Northwest Atlantic and Northeast Pacific Oceans. J. Phycol. **25**: 189–191.

STAVN, R. H. 1987. The three-parameter model of the submarine light field: Radiant energy absorption and trapping in nepheloid layers recalculated. J. Geophys. Res. **92**: 1934–1936.

———. 1988. Raman scattering effects in ocean optics, p. 131–139. *In* Ocean Optics 9, Proc. SPIE **925**.

VOSS, K. J. 1988. Radiance distribution measurements in coastal water, p. 56–66. *In* Ocean Optics 9, Proc. SPIE **925**.

———. 1989. Electro-optic camera system for measurement of the underwater radiance distribution. Opt. Eng. **28**: 241–247.

———, AND C. C. TREES. 1987. Differential optoacoustic absorption of pure water. Eos **68**: 1683.

———, AND G. ZIBORDI. 1989. Radiometric and geometric calibration of a visible spectral electro-optic "fisheye" camera radiance distribution system. J. Atmos. Ocean Technol. **6**: 652–662.

ZANEVELD, J. R. V., R. BARTZ, J. C. KITCHEN, AND R. W. SPINRAD. 1988. A reflective tube diffuse attenuation meter and absorption meter. Eos **69**: 1124.